High-mobility group nucleosomal binding domain 2 protects against microcephaly by maintaining global chromatin accessibility during corticogenesis

Received for publication, August 12, 2019, and in revised form, October 30, 2019 Published, Papers in Press, November 7, 2019, DOI 10.1074/jbc.RA119.010616

Xue-Ling Gao[‡§¶1], **Wen-Jia Tian**[§¶‖1], **Bofeng Liu**[‖**], **Jingyi Wu**[‖**2,3], **Wei Xie**[‖**], **and Qin Shen**[§¶‡‡4]

From the [‡]*School of Life Sciences, Peking University, Beijing 100871, the* [§]*Key Laboratory of Spine and Spinal Cord Injury Repair and Regeneration (Tongji University), Ministry of Education, Tongji Hospital, School of Life Sciences and Technology, Tongji University, Shanghai 200065, the* [¶]*Frontier Science Center for Stem Cell Research, Ministry of Education, School of Life Sciences and Technology, Tongji University, Shanghai 200092, the* [‖]*Tsinghua-Peking Center for Life Sciences, School of Life Sciences, Tsinghua University, Beijing 100084, the* **Center for Stem Cell Biology and Regenerative Medicine, MOE Key Laboratory of Bioinformatics, School of Life Sciences, Tsinghua University, Beijing 100084, and the* [‡‡]*Tongji University Brain and Spinal Cord Clinical Research Center, Shanghai 200092, China*

Edited by Xiao-Fan Wang

The surface area of the human cerebral cortex undergoes dramatic expansion during late fetal development, leading to cortical folding, an evolutionary feature not present in rodents. Microcephaly is a neurodevelopmental disorder defined by an abnormally small brain, and many gene mutations have been found to be associated with primary microcephaly. However, mouse models generated by ablating primary microcephaly-associated genes often fail to recapitulate the severe loss of cortical surface area observed in individuals with this pathology. Here, we show that a mouse model with deficient expression of high-mobility group nucleosomal binding domain 2 (HMGN2) manifests microcephaly with reduced cortical surface area and almost normal radial corticogenesis, with a pattern of incomplete penetrance. We revealed that altered cleavage plane and mitotic delay of ventricular radial glia may explain the rising ratio of intermediate progenitor cells to radial glia and the displacement of neural progenitor cells in microcephalic mutant mice. These led to decreased self-renewal of the radial glia and reduction in lateral expansion. Furthermore, we found that HMGN2 protected corticogenesis by maintaining global chromatin accessibility mainly at promoter regions, thereby ensuring the correct regulation of the transcriptome. Our findings underscore the importance of the regulation of chromatin structure in cortical development and highlight a mouse model with critical insights into the etiology of microcephaly.

Radial glial cells (RGCs)[5] in the embryonic ventricular zone are multipotent stem cells and the major source of cortical excitatory neurons, contributing to construction of the highly evolved neocortex. RGCs in the ventricular zone divide symmetrically to self-renew, expanding the ventricular surface laterally, or divide asymmetrically to generate neurons directly or indirectly via intermediate progenitor cells (IPCs) (1). In humans, it has been suggested that detachment of RGCs from the VZ to the outer subventricular zone leads to the generation of the outer RGCs, resulting in the expansion and folding of the neocortex (2). The cell fate determination and maintenance of RGCs are closely associated with their apical-basal polarity and cell cycle length (1). Extracellular matrix and apical junction complex are among the key components that establish and maintain the apical-basal polarity of RGCs (3).

Dysregulation of the division of RGs could lead to one of the most severe neural developmental disorders, microcephaly. This is defined as a significantly reduced occipito-frontal head circumference of more than three S.D. values below the mean of the same age, sex, and ethnicity, because normal head sizes vary greatly among individuals. The cause of microcephaly can be congenital or environmental, autosomal-recessive (autosomal-recessive primary microcephaly, MCPH), or associated with other genetic disorders (4). One difficulty in studying the etiology of microcephaly lies in the tolerance and variance of the human genome. As a healthy individual carries more than

This work was supported by National Science Foundation of China Grant 31671068 and Ministry of Science and Technology of China Grant 2019YFA0110102. The authors declare that they have no conflicts of interest with the contents of this article.
This article contains Table S1 and Figs. S1–S3.
The ATAC-sequence(s) and RNA-sequence(s) reported in this paper have been submitted to the NCBI Sequence Read Archive under BioProject under the accession number PRJNA534457.

[1] Both authors contributed equally to this work.
[2] Present address: Dept. of Pathology, Massachusetts General Hospital and Harvard Medical School, Boston, MA 02114.
[3] Present address: Broad Institute of MIT and Harvard, Cambridge, MA 02142.
[4] To whom correspondence should be addressed. E-mail: shenqin@tongji.edu.cn.

[5] The abbreviations used are: RGC, radial glial cell; IACUC, institutional animal care and use committee; IPC, intermediate progenitor cell; VZ, ventricular zone; SVZ, subventricular zone; RG, radial glia; MCPH, autosomal-recessive primary microcephaly; ASPM, abnormal spindle-like microcephaly-associated; HMGN, high-mobility group nucleosomal binding domain; HMG, high-mobility group; KLF7, Kruppel-like factor 7; CCNB1, cyclin B1; E, embryonic day; P, postnatal day; KO, knockout; mKO, microcephalic KO; BrdU, bromodeoxyuridine; pH3, phosphorylated histone H3; OCR, open chromatin region; TF, transcriptional factor; GSEA, gene set enrichment analysis; RXR, retinoid X receptor; GW, gestational week; KOMP, Knockout Mouse Project; PFA, paraformaldehyde; NP-40, Nonidet P-40; HRP, horseradish peroxidase; DEG, differentially expressed gene; FDR, false discovery rate; GO, gene ontology; DAPI, 4′,6-diamidino-2-phenylindole; FPKM, fragments per kilobase of exon model per million reads mapped; EGFP, enhanced green fluorescent protein.

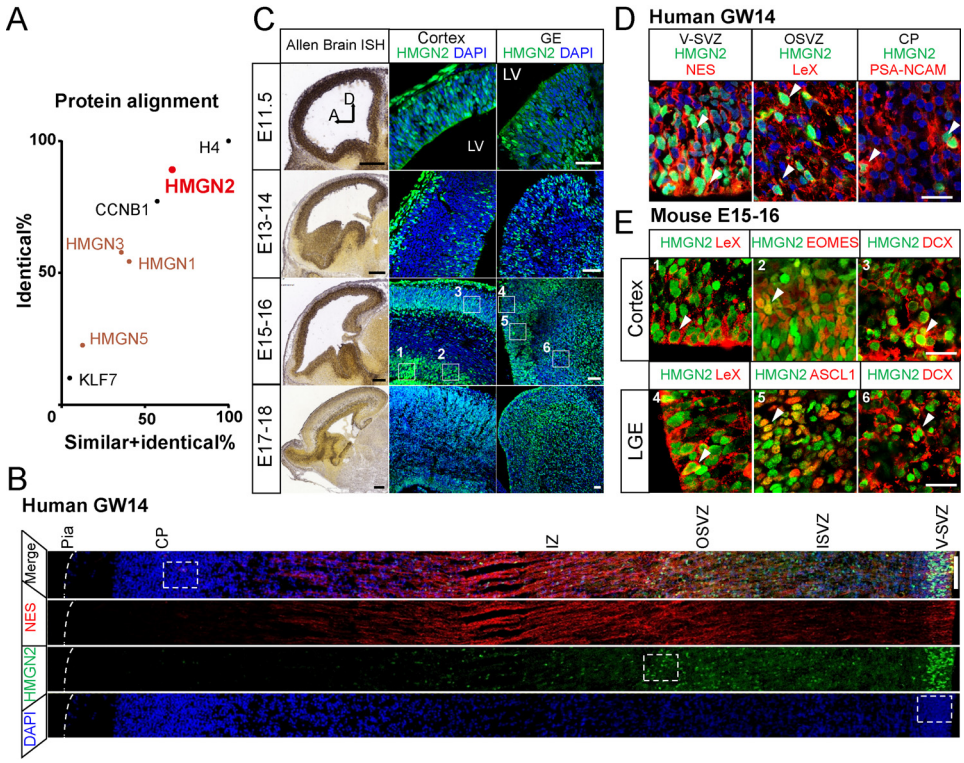

Figure 1. Expression pattern of *Hmgn2* in the embryonic brain is conserved in human and mouse (see related Fig. S1). *A*, local alignment of HMGN proteins among six vertebrates (human, cow, rhesus monkey, rat, mouse, and African clawed frog) using the Clustal Omega program. *x* and *y* axes indicates the percentage of similar or identical amino acids in the total sequences. *KLF7*, *CCNB1*, and *H4* are gene symbols of Kruppel-like factor 7 (KLF7), cyclin B1 (CCNB1), and histone H4. *B*, immunostaining of HMGN2 in human fetal cerebral cortex (gestational week 14, GW14). *V-SVZ*, ventricular-subventricular zone; *ISVZ*, inner subventricular zone; *OSVZ*, outer subventricular zone; *CP*, cortical plate. *C*, continuous expression of HMGN2 in mouse forebrain neurogenic regions from E11.5 to E18. *Left*, images of *in situ* hybridization from the Allen Brain Atlas; *middle*, images of immunostaining in the cerebral cortex; *right*, images of immunostaining in the ganglionic eminence (*GE*); all of HMGN2. *D*, dorsal; *V*, ventral; *LV*, lateral ventricle. *D*, magnified images of the *boxed areas* in *B*. *Arrowhead*, double-positive cells for labeled markers. *NES* or *LeX*, radial glial marker; *PSA-NCAM*, newborn neuron maker. *E*, co-expression of HMGN2 and cell type–specific markers in the mouse brains at E15-E16 around the regions comparable with the boxed areas (*1–6*) in *D*. *LGE*, lateral ganglionic eminence. Shown are radial glia (*left*) (LeX^+), intermediate progenitor cells (*middle*) ($EOMES^+$ or $ASCL1^+$), and immature neurons (*right*) (DCX^+). *Scale bars*, 200 μm (*B*), 20 μm (*C* and *E*), and 400 μm (*D*, *left column*), 50 μm (*D*, *middle* and *right columns*).

46 nonsense mutations on average (5), 3–24 disease-causing mutations in homozygous state (6), and multiple copy number variations (7), identifying microcephaly-associated genes is extremely challenging, not to mention the fact that the phenotype spectrum of patients with MCPH gene mutations is wider than previously suggested (4). Another difficulty lies in the evolutionary divergence between humans and mice. Although mutations in MCPH genes such as *ASPM* (abnormal spindle-like microcephaly-associated) have been identified in microcephaly patients, mice deficient in these genes sometimes only show mild abnormality (8–10).

Emerging evidence has suggested the importance of chromatin remodelers in central nervous system development (11, 12), whereas it remains to be investigated whether the change of global chromatin state is associated with neocortical development and whether this change could drive the differentiation of embryonic radial glia (13–15). High-mobility group nucleosomal binding domain (HMGN) is a family of nucleosome-binding proteins, of which the two major variants, HMGN1 and HMGN2, have been shown to affect histone modification and play a role in the establishment and maintenance of regulatory sites in chromatin (16). Knockout of either *Hmgn1* or *Hmgn2* induces several mild abnormalities in mice, due to the functional compensation for HMGN variants (17). Interestingly, *Hmgn2* is predicted to be highly likely haploinsufficient in the human genome (18, 19) and is known to be included in a heterozygous copy number variation duplication of seven genes in a patient with microcephaly (DECIPHER ID 256762) (20). Therefore, we designed experiments to determine whether HMGN2 plays a role in corticogenesis and whether this is accomplished by maintaining global chromatin accessibility in mice.

Results

HMGN2 is highly conserved and abundantly expressed in embryonic brain of humans and mice

The high-mobility group (HMG) family includes the *HMGN*, *HMGA*, and *HMGB* genes. The HMGN protein family comprises *HMGN*1–5 in humans and *Hmgn*1, -2, -3, and -5 in mice (21). We performed protein alignments to compare the conservation of protein sequences in HMGNs among six vertebrates (Fig. 1*A*). HMGN2 was the most conserved protein in the HMGN family, with higher scores than the two essential protein references, Kruppel-like factor 7 (KLF7) and cyclin B1 (CCNB1) (22), suggesting an important function. We then examined the expression pattern of *HMGN*2 in the developing forebrain of humans and mice by immunostaining and found that it was expressed in the V-SVZ and the cortical plate in humans at

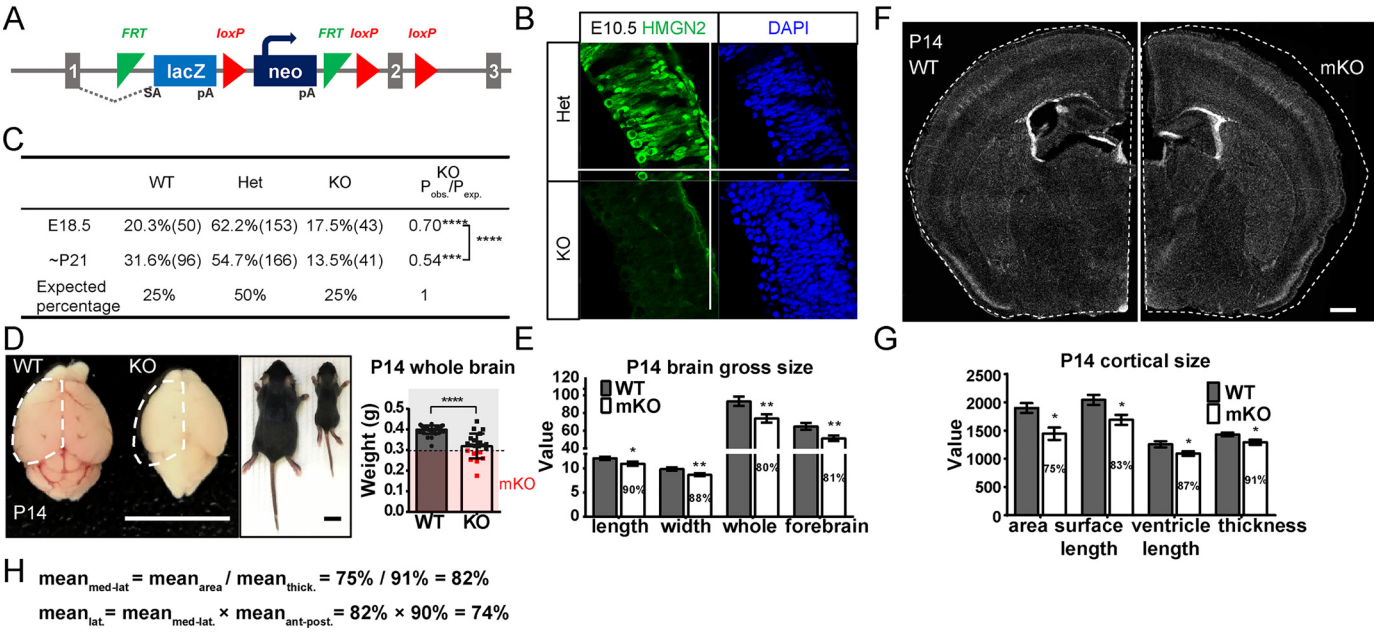

Figure 2. *Hmgn2* deficiency in mice causes microcephaly with features of human microcephaly (see related Fig. S2). *A*, diagram of the construction of the *Hmgn2*-knockout allele (*Hmgn2*$^{tm1a(KOMP)Wtsi}$) from KOMP. The complete coding sequence of *Hmgn2* is silenced, and lacZ is expressed instead. *B*, images of immunostaining of HMGN2 in the cerebral cortex at E11.5 of WT and KO mice. The *green signal* in the KO cortex is autofluorescence from blood vessels and the pia. *C*, *table* of genotype distributions of the progeny of in-bred heterozygotic parents at E18.5 and at weaning, along with the expected Mendelian distribution. The percentage of each genotype is listed, with the corresponding number of mice in *parentheses*. The KO survival rate decreased dramatically at E18.5 and further decreased at weaning (comparisons assessed using the χ^2 test). *D*, photographs of the brain and body *Hmgn2*-KO and WT mice at P14. The cortical area of the WT hemisphere circumscribed by the *dashed line* was superimposed onto the KO brain to show the reduction in brain size. The threshold of microcephaly, which is defined by brain weight $<$ ($mean_{WT} - 3S.D._{WT}$), is shown as the *dashed line* in the bar graph. Mice with brain weights below the threshold were categorized as mKO (*labeled* in *red*). Data indicate mean $\pm$ S.D. (*error bars*) (WT, $n = 36$; KO, $n = 21$). *E*, measurements of the WT and mKO brains at P14 by length (anterior-to-posterior), width (medial-to-lateral), and whole-brain and forebrain "area" (*i.e.* the area occupied by the corresponding structure from photographs of the dorsal aspect of the brain of P14 mice). Units for each group of *columns* in order are as follows: 1 mm, 1 mm, 1 mm^2, 1 mm^2 (WT, $n = 5$; KO, $n = 6$). *F*, coronal sections from WT and mKO P14 mice stained with DAPI (*white*). *G*, area, surface length, ventricular length, and thickness (from the ventricular surface to the pial surface) of the neocortex of P14 WT and mKO mice at an anterior-posterior position similar to that in *F*. mKO brains show more marked reduction laterally than radially. Units for each group of columns in order are as follows: 10^4 μm^2, 10 μm, 10 μm, 1 μm (WT, $n = 4$; KO, $n = 4$). *H*, equations of the mean mediolateral length of the neocortex in the coronal section and the mean lateral expansion of the cortex, presented by the percentage of mKO relative to WT. *C–G*, data indicate mean $\pm$ S.E. (*error bars*) if not specified. *, $p < 0.05$; **, $p < 0.01$; ***, $p < 0.001$; ****, $p < 0.0001$, paired Student's *t* test for *E* and unpaired Student's *t* test for the rest. *Scale bars*, 20 μm (*B*), 1 cm (*D*), and 500 μm (*F*).

gestational week 14 (GW14) and throughout the embryonic stages in mice (Fig. 1, *B* and *C*). Specifically, RGCs expressing NES and LeX were positive for HMGN2 in human V-SVZ and the outer SVZ (Fig. 1*D*) and in the mouse VZ (Fig. 1*E*). HMGN2 was also detected in IPCs, which were labeled by the specific markers EOMES and ASCL1, and in newborn neurons expressing the neuronal markers PSA-NCAM or DCX in both species (Fig. 1, *D* and *E*). In cortical cells of embryonic day 0.5 14.5 (E14.5) mice and GW13 humans, the transcriptomic profiles of all canonical HMG genes show a very similar pattern (23) (Fig. S1, *A–D*).

In postnatal mice, HMGN2 was continuously expressed in the SVZ of the lateral ventricle and the subgranular zone of the hippocampal dentate gyrus, where adult neurogenesis takes place (Fig. S1*E*). In adults, HMGN2 was expressed in both GFAP$^+$ cells and newborn neurons expressing PSA-NCAM in the SVZ and subgranular zone (Fig. S1*F*). In summary, HMGN2 is conserved not only in terms of the protein sequence but also in its expressional profile in the embryonic cortex in both humans and mice.

Ablating Hmgn2 is subviable for mice in embryonic and postnatal stage

Based on the conservation of the protein sequence and the expression pattern of HMGN2 in human and mouse brain, we hypothesized that investigation of the function of HMGN2 in mouse brain development may shed light on understanding its function in human brain development and diseases. To test this hypothesis, we obtained an *Hmgn2*-KO mouse line, *Hmgn2*$^{tm1a(KOMP)Wtsi}$, generated by the Knockout Mouse Project of the University of California (Davis, CA) (24). The mutant allele was initially generated as a nonexpressive form by inserting a poly(A) signal before the coding sequence of *Hmgn2* (Fig. 2*A*). The knockout efficiency was nearly 100% by E10.5, as shown by immunostaining (Fig. 2*B*), further verified by Western blotting on E14.5 and by RNA-Seq on postnatal day 14 (P14) (Fig. S2, *A* and *B*). We inbred the heterozygous *Hmgn2*^{tm1a} and systematically analyzed the genotypes of 250–300 offspring to see if they followed Mendel's law (Fig. 2*C*). At E18.5, in contrast to the theoretical Mendelian rate of 25%, only 17.5% of the embryos recovered were KO mice, meaning that the viability of the KO embryos was only ~70%. By weaning, the survival rate of KO mice had decreased further to 54%. Hence, *Hmgn2* is a subviable gene satisfying the definition in a previous report for the variable lethality after knockout (22, 25). Our result indicates that *Hmgn2* is essential for both embryonic and postnatal development with incomplete penetrance.

Hmgn2 deficiency leads to microcephaly in the mouse model

The KO pups died from birth to weaning, with a peak during the first 2 days. We found that the total brain weight was significantly reduced at P14 in KO mice, which also exhibited growth retardation (Fig. 2*D* and Fig. S2*C*), with a larger variation than the WT mice. The growth retardation was consistent with many other mouse models of depletion of MCPH genes (8–10). The definition of human microcephaly is a head circumference that is <3 S.D. values from the mean of normal infants; here, we defined microcephalic KO (mKO) mice as those with brain weights < 3 S.D. values from the mean of WT brains. According to this criterion, we found that microcephaly was manifested in ~30% of the KO mice (Fig. 2*D*), which did not survive to P21, indicating incomplete penetrance and variable expressivity, which is often the case for human diseases (26). To better illustrate the working mechanism of how losing *Hmgn2* caused microcephaly, we further analyzed and compared mKO brains with WT brains as they were abnormal vera. We found that mKO brains had decreased size, with similar reductions in the cortical anterior-to-posterior and medial-to-lateral axes (*length* and *width* in Fig. 2*E*). The degree of reduction in mediolateral length from anterior to posterior did not vary much (Fig. S2*D*), so we selected the position around bregma −0.46 to precisely measure the reduction in the length along medial-to-lateral axes (cortical length) and in cortical thickness in brain sections (Fig. 2*F*). We found that the neocortical thickness in mKO mice was reduced to 91% of the WT, whereas the reduction in cortical ventricular length (87% of WT) and cortical surface length (83% of WT) was greater. Because both anteroposterior and mediolateral length contribute to the lateral expansion of the cerebral cortex, the decrease in lateral expansion (74% of WT) was more responsible than radial expansion (cortical thickness, 91% of WT) for the microcephaly of mKO mice (Fig. 2*H*). This phenomenon was consistent with what was observed in human microcephaly patients and the ferret ASPM-knockout model (2), suggesting that the RGCs responsible for cortical expansion may be lost in mKO mice.

Microcephalic KO mice retain generally normal radial corticogenesis

During cortical histogenesis, NSCs produce neurons in an inside-out pattern sequentially from the deeper layers to the upper layers, resulting in radial expansion. We then investigated whether cell number and neuron production in a radial unit (an RGC and its progeny) is affected in P14 mKO mice. We found that neither the number of cell nuclei nor $CUX1^+$ neurons changed significantly per unit of ventricular length in mKO compared with that in WT mice (Fig. 3 (*A* and *B*) and Fig. S2*H*). Consistently, the production of upper-layer neurons labeled by bromodeoxyuridine (BrdU) injection at E15.5 was not changed per unit of ventricular length in *Hmgn2*-null mice when analyzed at P14 (Fig. 3, *C* and *D*). In addition, we found that $BrdU^+$ neurons reached the correct positions in the upper layers in mKO mice (Fig. 3, *C* and *E*), and the distribution of the layer markers CUX1, CTIP2, and SATB2 in mKO mice was similar to that in WT mice (Fig. 3*A*), suggesting that cortical lamination was normal in mKO. Notably, cell density in the entire cortex or different cortical regions in mKO mice was not significantly different from that in the WT; however, in layers V/VI, the cell density was higher. As the number of deeper layer cells was not changed (Fig. S2*E*) in mKO mice, this increase in density could be explained by the reduced thickness of layers in mKO mice (Fig. S2, *F* and *G*). Our results indicate that within an expanding radial unit, the generation and migration of neurons are not affected by *Hmgn2* deficiency. However, as the ventricular length was reduced, the overall cell number was decreased, leading to a microcephalic phenotype.

To determine whether gliogenesis was affected by loss of *Hmgn2*, we labeled the entire lineage of E15.5 RGCs with the piggyBac-transposon system by *in utero* electroporation. This system, consisting of a helper plasmid expressing piggyBac transposase (PBase) and a piggyBac donor plasmid (PB-GFP), enables the stable integration of donor genes into all progeny of E15.5 RGs after plasmid transfection (27). Glia were distinguished from neurons according to morphology labeled by GFP. The ratio of glial cells in GFP^+ cells was higher in P14 mKO mice than in the WT (Fig. 3, *F* and *G*). In addition, stunted littermates with KO already exhibited microcephaly (Fig. S2*I*) before gliogenesis reached its peak (28, 29), indicating that microcephaly in *Hmgn2* mKO mice is not caused by glia loss. We found very little cleaved caspase-3 staining in P4 and P14 mKO cortex (Fig. S2*J*), suggesting that cell death does not account for the microcephaly in *Hmgn2*-null mice. Taken together, due to a reduction in overall lateral expansion, mKO mice exhibit microcephaly despite the generally normal production of cortical cells within a radial unit.

Loss of Hmgn2 results in enhanced differentiation and altered cell division of radial glial cells

As *Hmgn2*-deficient mice were underrepresented at E18.5, we determined whether microcephaly had already taken place by that time. The average brain weight at this stage was significantly lower in the KO group, and some mice also met the criteria for mKO (Fig. 4, *A* and *B*). The cortical area and surface length were significantly lower in mKO mice, whereas cortical thickness and ventricular length did not differ from the WT (Fig. 4*C*). Both the thickness of VZ and SVZ expanded, whereas the cortical plate was thinner in mKO mice (Fig. 4*D*). Consistently, the number of deeper-layer neurons ($CTIP2^+$) decreased (Fig. 4, *E* and *F*), suggesting that early neurogenesis (before E14.5) was attenuated. Whereas the RG ($PAX6^+$) pools did not change in mKO mice, the IPCs ($EOMES^+$) and the transitional cell type ($PAX6^+$ $EOMES^+$) expanded in E18.5 mKO mice, suggesting that the self-renewal of RGs was attenuated (Fig. 4, *G* and *H*). Notably, ectopic IPCs and $PAX6^+$ $EOMES^+$ transitional cells that appeared outside the V-SVZ dramatically increased in mKO mice (Fig. 4*H*), suggesting that the progenitor cells were displaced from their original niche. The precocious withdrawal of VZ neural progenitors from the germinal zones is reminiscent of the $ASPM^{-/-}$ ferret model of microcephaly.

We next assessed the proliferative behavior of cortical radial glia in E18.5 mKO cortex. First, we found that the proportion of progenitor cells on the surface of the ventricle in M-phase (labeled by the phosphorylated histone H3, pH3)

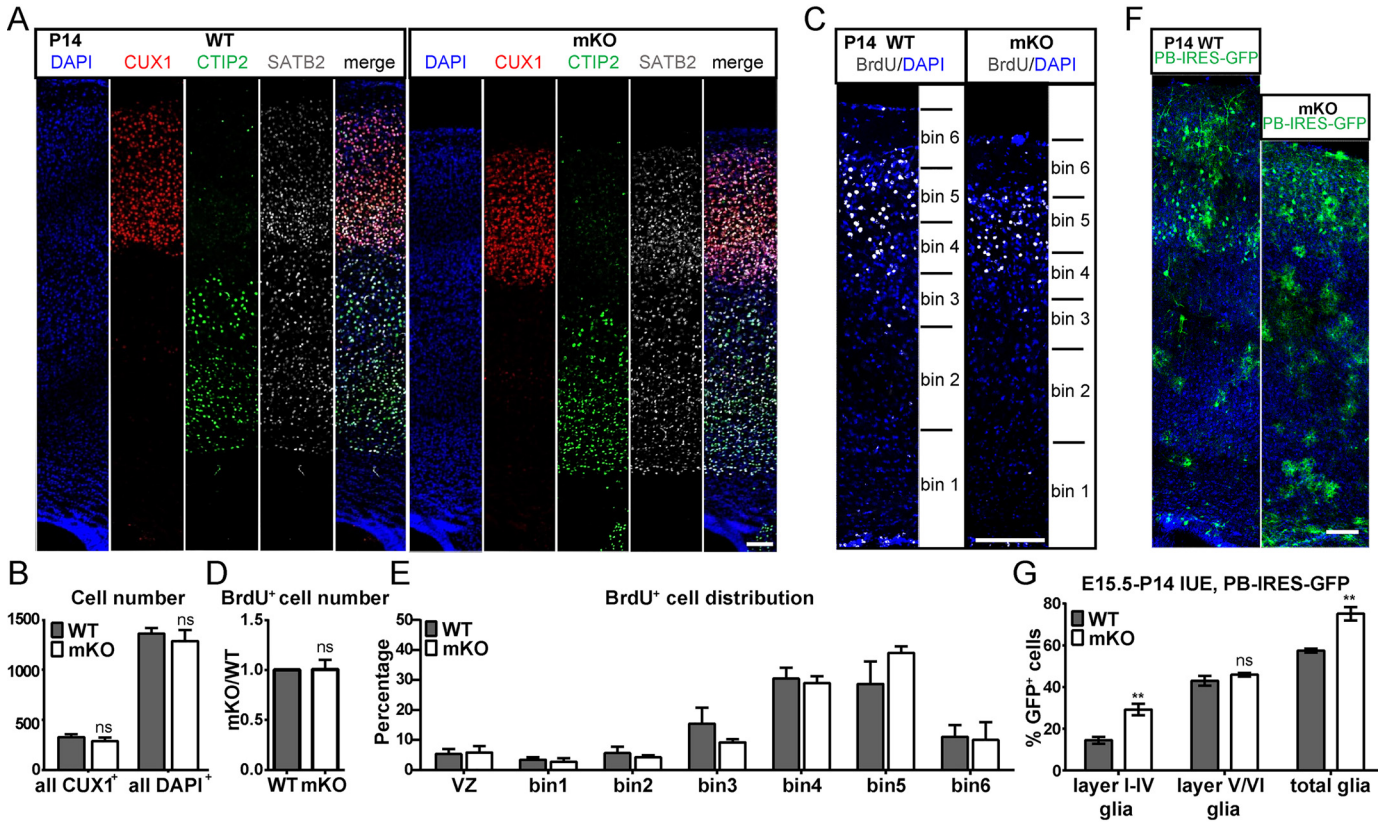

Figure 3. Total cell number (neurons + glia) in the cerebral cortex are reduced in KO-*Hmgn2* mice with microcephaly (see related Fig. S2). *A*, images of immunostaining to label nuclei (DAPI), layer II–IV neurons (CUX1), layer V/VI neurons (CTIP2), and callosal projection neurons (SATB2) in P14 coronal brain sections. *B*, quantification of the cell number per 100-μm width of cortex as in *A* (WT, $n = 5$; KO, $n = 4$). *C*, representative image of P14 cortex stained for BrdU, which was injected at E15.5. Each of bins 1 and 2 occupies one-fourth of the cortical width; each of bins 3–6 occupies one-eighth of the cortical width. *D*, quantification of the number of BrdU$^+$ cells per 100-μm width of cortex. For each batch of mice, KO was normalized to its corresponding WT ($n = 3$). *E*, the percentage of BrdU$^+$ cells distributed in each bin illustrated in *C* ($n = 3$). *F*, representative images of P14 WT and mKO cortex transfected with a piggyBac-transposon system expressing EGFP by *in utero* electroporation at E15.5. *Green cells* were all progeny of E15.5 radial glial cells. *G*, percentages of glia in the E15.5 progeny at P14 as in *F*. Cells were categorized as neurons or glia by morphology ($n = 3$ for each genotype). *B–G*, data show mean ± S.E. (*error bars*). *, $p < 0.05$; **, $p < 0.01$; *ns*, not significant, unpaired Student's *t* test. *Scale bars*, 100 μm in *A*, *C*, and *F*.

was higher in mKO than that in WT mice (Fig. 4, *I* and *J*). We then measured the fraction of dividing cells along the ventricular surface in prophase and pro-metaphase *versus* those in metaphase, anaphase, and telophase, reflecting the progression of mitosis. We found that the fraction of prophase/pro-metaphase cells increased in mKO mice (Fig. 4, *I″* and *K*), indicating that the duration of prophase/pro-metaphase was prolonged. Therefore, the increase in the number of pH3$^+$ RGCs was more likely caused by cell-cycle delay rather than increased proliferation. Furthermore, more ventricular RGCs with an oblique spindle orientation were detected in mKO than in WT mice (Fig. 4*L*), indicating that fewer ventricular RGCs underwent symmetrical cell divisions, which may lead to decreased self-renewal of RGs and further the decrease in cortical lateral expansion. RGCs with more oblique orientation of the cleavage plane could leave the ventricular zone (30), explaining the detachment of IPCs and PAX6$^+$ EOMES$^+$ transitional cells.

Hmgn2 deficiency impairs gene expression by diminishing global chromatin accessibility

To determine how HMGN2 protects against microcephaly, we evaluated the global chromatin accessibility and its influence on the transcriptome of WT and mKO cortical cells at P14 using an assay for transposase-accessible chromatin followed by sequencing (ATAC-Seq) (31) and RNA-Seq. To identify the features of HMGN2 targeting specificity, we analyzed the deep-sequencing data of ChIP-HMGN2 in neural progenitor cells differentiated from mouse embryonic stem cells based on a previous study (17). We found that HMGN2 predominantly bound to gene promoter regions (54% of 25,594 total peaks of 12,684 genes Fig. S3*A*), and this binding was associated with greater chromatin accessibility and higher transcriptional activity in WT P14 cortical cells (Fig. S3, *B* and *C*).

Using ATAC-Seq, we captured 29,217 peaks as open chromatin regions (OCRs; Fig. 5*A*) in P14 WT cortical cells. Compared with the WT, mKO cortical cells had significantly fewer OCRs (22,511 peaks, 77% of the WT) and dramatically reduced signals of ATAC-Seq at transcription start sites (Fig. 5, *A* and *B*). The reduction of OCRs mainly occurred at promoters, consistent with the binding preferences of HMGN2. Furthermore, the chromatin accessibility greatly reduced at HMGN2-binding sites (Fig. 5*C*), indicating that HMGN2 indeed maintains the OCRs it binds accessible for regulatory elements, such as transcriptional factors (TFs). The overall reduction in chromatin accessibility resulted in the up-regulation of 798 genes and

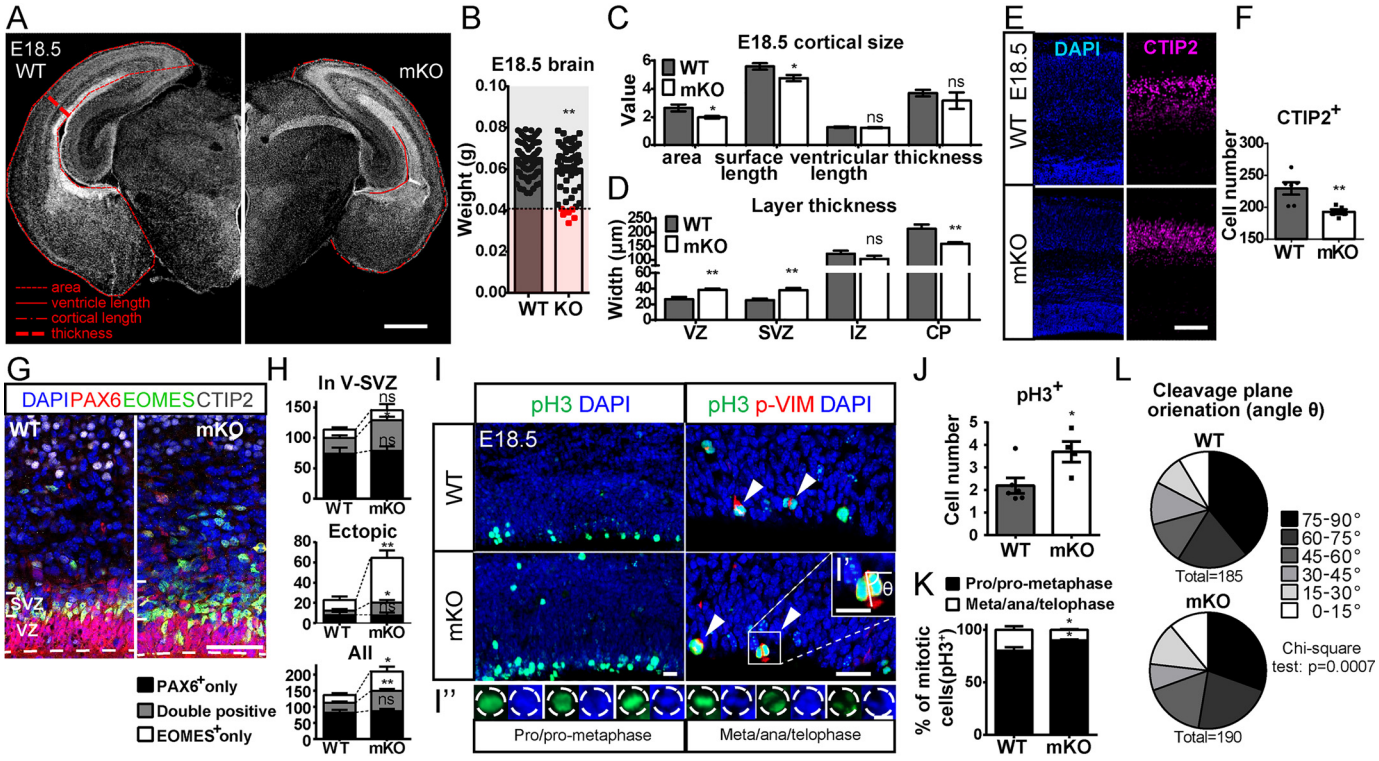

Figure 4. Loss of *Hmgn2* results in altered cell division and radial glial cell fate. *A*, coronal sections of E18.5 WT and mKO mice stained for DAPI. *B*, statistics of whole-brain weight of all WT and KO mice at E18.5 after perfusion (WT, $n = 85$; KO, $n = 58$). KO brains were significantly lighter than those of the WT. Brains below the threshold were defined as mKO (*labeled* in *red*). *C*, the area, surface length, ventricular length, and thickness of neocortex in E18.5 WT and mKO mice at an anterior-posterior position similar to that in *A*. The measurements are indicated by *red outlines* in *A*. Units for each column in order are as follows: 10^6 μm^2, 10^3 μm, 10^3 μm, and 100 μm. Data indicate mean ± S.E. (*error bars*) ($n = 6$ for each genotype). *D*, thickness of the ventricular zone (*VZ*), subventricular zone (*SVZ*), intermediate zone (*IZ*), and cortical plate (*CP*) in E18.5 WT and mKO cortex, determined by PAX6/EOMES/DAPI staining ($n = 6$ for each genotype). *E*, images of immunostaining for the layer V/VI neuron marker, CTIP2, and the nuclear marker, DAPI, on E18.5 coronal brain sections. *F*, numbers of $CTIP2^+$ layer V/VI neurons per 100 μm of ventricle length in WT and mKO mice, as in *E* (WT, $n = 6$; KO, $n = 5$). *G*, confocal images of E18.5 coronal brain sections co-stained for nuclei (DAPI), radial glia (PAX6), IPCs (EOMES), and layer V/VI neurons (CTIP2). *Dashed lines* outline the ventricular surfaces. VZ and SVZ are indicated by *solid lines*. *H*, numbers of cells expressing PAX6 or EOMES and the transitional cell type expressing both markers in the V-SVZ, outside the V-SVZ (ectopic), and their sum (WT, $n = 5$; KO, $n = 4$). *I*, images of co-staining of pH3, phosphor-Vimentin (*p-VIM*), and DAPI to identify mitotic radial glia at E18.5 in WT and mKO cortex. *Right*, representative confocal images of radial glia in anaphase. Cleavage plane orientation was measured as the angle θ between the cleavage plane and the VZ surface, illustrated by a further 2× magnification in (*I'*). High-magnification images of prophase/pro-metaphase and meta/ana/telophase cells are shown in (*I''*). *J*, numbers of M-phase radial glia per 100 μm along the apical surface of the ventricle in E18.5 WT and mKO cortex (WT, $n = 6$; KO, $n = 4$). *K*, proportions of mitotic cells in prophase/pro-metaphase (*black*) *versus* meta/ana/telophase (*white*) (WT, $n = 6$; KO, $n = 4$). *L*, cleavage orientation of radial glia in anaphase and telophase along the ventricle in E18.5 WT and mKO cortex. *Scale bars*, 500 μm (*A*), 100 μm (*E*), 50 μm (*G*), 20 μm (*I*), and 10 μm (*I'* and *I''*). *B–L*, data indicate mean ± S.E. (*error bars*) *, $p < 0.05$; **, $p < 0.01$; ***, $p < 0.001$; ****, $p < 0.0001$; *ns*, not significant, unpaired Student's *t* test.

down-regulation of 592 genes revealed by RNA-Seq (Fig. 5*D*). The number of up-regulated genes that were directly targeted by HMGN2 was nearly the same as that of down-regulated genes (Fig. 5*E*), suggesting that during corticogenesis, HMGN2 serves as a modulator of transcription rather than an activator or repressor. In agreement, compared with all expressed genes, the chromatin accessibility of the transcription start sites of HMGN2-targeted genes (both the up- and down-regulated) was more susceptible to *Hmgn2* depletion (Fig. 5*F*). Chromatins of differential expressed genes that were targeted by HMGN2 were not as closed as all targeted genes, probably because this relatively open state was beneficial for, or even the consequence of, the approach of TFs and chromatin remodelers to modulate transcription. Taken together, the binding of HMGN2 guarded genome-wide chromatin accessibility predominantly around transcriptional start sites, ensuring both transcription activation and suppression of targeted genes during corticogenesis.

HMGN2 regulates functional gene sets to protect against microcephaly

We next looked for the causes of microcephaly after HMGN2 ablation using gene ontology analysis and gene set enrichment analysis (GSEA). The functional classification of up-regulated genes by gene ontology analysis resulted in an enrichment of terms relating to neuronal activity, suggesting dysregulated neuronal differentiation (Fig. 6*A*). The terms proteinaceous extracellular matrix, cell adhesion, and apical plasma membrane were highly enriched in the genes that were down-regulated after *Hmgn2*-KO, and genes for apical junction assembly were generally down-regulated in mKO cells (Fig. 6*B*). The above data explained why the spindle orientation of dividing RGs and the displacement of neural progenitor cells occurred in E18.5 mKO cortex, given that apical junctions and extracellular matrix of RGCs play an important role in maintaining RG cell fate (32). Surprisingly, neither the overall nor individual expression level of microcephaly-associated genes

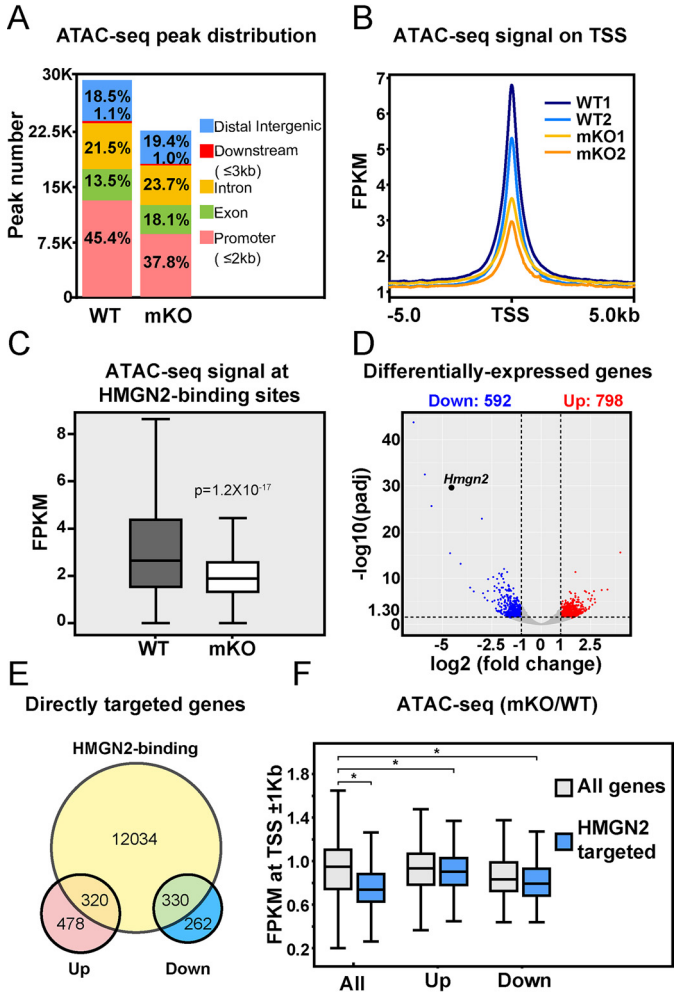

Figure 5. HMGN2 functions by maintaining global chromatin accessibility (see related Fig. S3). *A*, distributions of ATAC-Seq peaks across the genome of P14 WT and mKO cortex. The percentages of ATAC-Seq peaks mapping within each category of genomic region are indicated. *B*, ATAC-Seq enrichment profile within a 10.0-kb genomic window centered on the transcription start site (*TSS*) of P14 WT (*blue*) and mKO (*yellow*) cortical cells, each showing two biological replicates. *C*, volcano plot of the distribution of the -fold change expression (*x axis*) and the adjusted *p* value (*y axis*) of genes differentially expressed in WT and mKO cortex at P14 (*blue*, down-regulated genes; *red*, up-regulated genes). Differentially expressed genes were defined by $|\log_2(\text{-fold change})| > 1$; adjusted *p* value < 0.05 (WT, $n = 2$; KO, $n = 3$). *D*, the ATAC-Seq signal at the HMGN2 binding sites of P14 WT and mKO mice. *E*, Venn diagram showing the intersections of HMGN2-binding genes, up-regulated genes, and down-regulated genes in the mKO cortex. Genes in the intersections were considered directly regulated by HMGN2, whereas the others could be indirectly regulated. *F*, box plot showing the ratio of the FPKM of the ATAC-Seq signal of mKO to that of the WT within ±1 kb of the TSS for all expressed genes, up-regulated genes, and down-regulated genes; all (*gray*) or directly targeted by HMGN2 (*blue*). *, $p < 10^{-33}$; unpaired Student's *t* test. Whiskers of box plots, the first quartile minus 1.5 fold inter-quartile range (*down*) and the third quartile plus 1.5 fold inter-quartile range (*up*).

was decreased in mKO compared with WT cells (Fig. S3*D*). Rather, the expression of genes responsible for stem cell proliferation was down-regulated in mKO cells, indicating that the appearance of increased numbers of neural progenitor cells in V-SVZ of E18.5 mKO cortex was unlikely to be the result of an increase in proliferation. We found that 15 essential genes identified in a mouse knockout study (22) were down-regulated in mKO cells (Fig. S3*E*), elucidating the cause for the lower survival rate of *Hmgn2*-null mice.

As 1000 genes greatly changed their expression in mKO cortical cells, and dozens of genes are responsible for cell proliferation, it is conceivable that HMGN2 regulates a cohort of downstream effectors during neocortical development. By searching genes from the GO terms "cilium movement" and "cell proliferation," We found three possible direct downstream effectors that meet the following three criteria: expressed in embryonic neocortical neural progenitor cells, the promoters of which HMGN2 binds to, and with decreased chromatin accessibility and transcription level in mKO cells (Fig. 6, *C* and *E*). Klf4 and Jag1 are required for the maintenance of radial glia and cell proliferation (33, 34). Cep85, on the other hand, protects centriole duplication, PLK4 activation, and the efficient centriolar targeting of STIL and SASS6, both of which are microcephaly-associated genes (35). On the other hand, proneural genes *Neurod1*, *Neurod2*, and *Neurod6* were all up-regulated (only *Neurod1* was directly targeted), but without clear changes in ATAC-Seq signal. As NeuroD genes are expressed mainly in postmitotic neurons and ectopic expression of NeuroD genes in progenitor cells causes cell cycle withdraw by up-regulating cell cycle inhibitors and down-regulating cell cycle progression factors (36–38), they were also likely to be responsible for the mKO phenotype.

We further explored whether HMGN2 binds to the sites where specific TFs are located during neural stem cell development and whether these TFs bind the three predicted direct downstream effectors. We identified abundant and significant enrichment of KLF7, RBPJ, retinoid X receptor (RXR), and NFYA at the HMGN2-binding sites using *de novo* motif analysis (Fig. 6*D*). *Klf7* is an essential gene for mouse embryonic development and important for neuronal morphogenesis (22, 39, 40). RBPJ is a TF that plays a central role in Notch signaling and is essential for the maintenance of neural stem cells during corticogenesis (41). RXRs affect proliferation of neural progenitors (42) and are among the receptors of retinoic acid signaling which is a key signaling controlling the symmetric to asymmetric division of neural stem cells during corticogenesis (43). NF-Y is important for mouse early neural development, cell proliferation, and chromatin accessibility (44–46). Consistently, we found that these motifs were predicted to be located within the HMGN2-binding sites of the three potential target genes (Fig. 6*E*).

In conclusion, HMGN2 binds mainly to promoter regions in the genome, maintaining the global chromatin accessibility of P14 cortical cells for proper transcription. Furthermore, we propose that HMGN2 preferentially binds to the sites occupied by TFs of key signaling pathways of RGC development, facilitating the approach of these TFs to the downstream executors, and consequently maintains their transcription as well as functions against microcephaly.

Discussion

In this study, we suggest that the expression of HMGN2 in neocortex is required for maintaining cortical volume, especially proper lateral expansion. HMGN2 preserves neurogenesis by maintaining the self-renewal of apical RGCs, possibly by maintaining their localization and mitotic progress. We demonstrate that HMGN2 maintains chromatin accessibility in

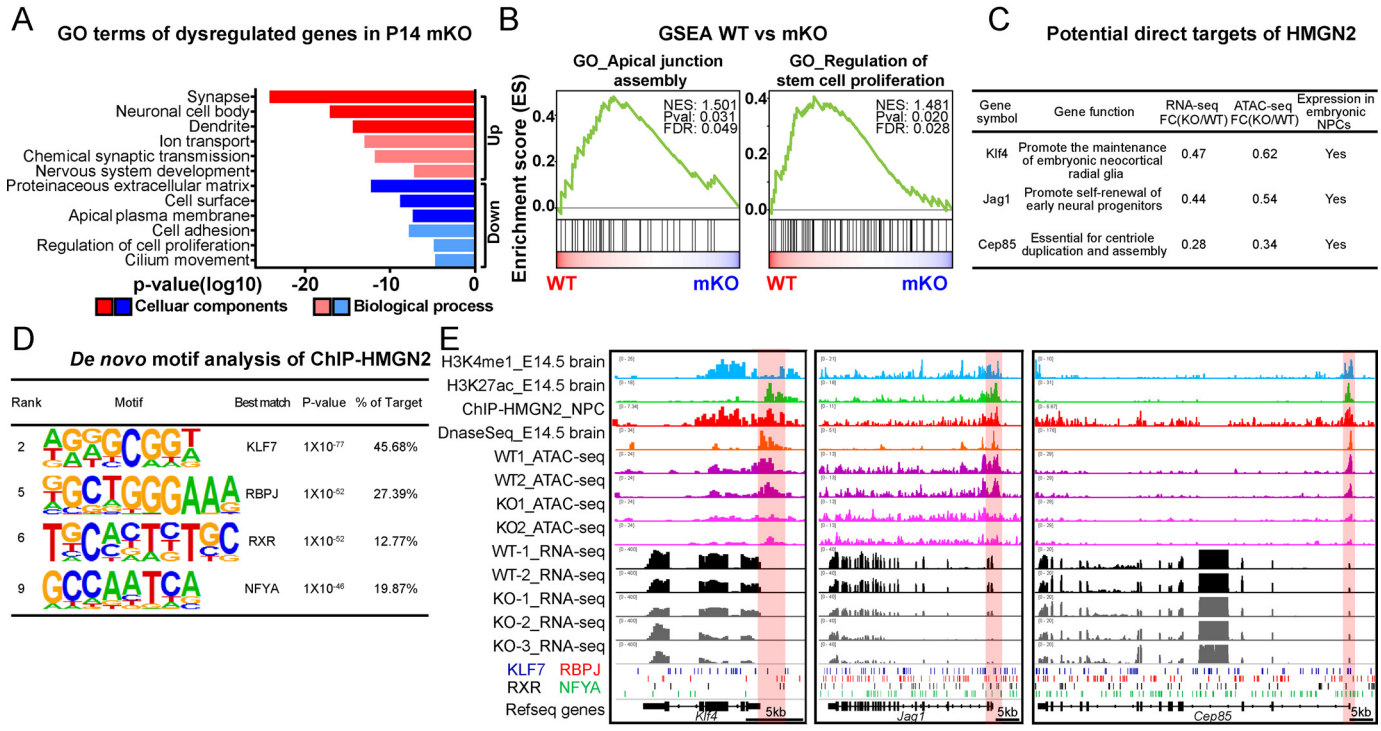

Figure 6. HMGN2 is predicted to integrate functional signaling pathways to potential targets. *A*, GO of up-regulated and down-regulated genes in mKO compared with WT. GO terms are plotted as the negative logarithm of their *p* value. *B*, GSEA of "apical junction assembly" and "regulation of stem cell proliferation" in mKO *versus* WT P14 cortical cells (WT, $n = 2$; KO, $n = 3$; expression of all genes was analyzed). *NES*, normalized enrichment score. *C*, potential downstream genes responsible for microcephaly in *Hmgn2*-null mice, selected among the down-regulated genes in mKO. -Fold change (*FC*) "expression" for RNA-Seq and ATAC-Seq of each gene calculated by DESeq2 is listed. *D*, *de novo* identification of motifs under HMGN2-binding sites using Homer (threshold: percentage of target >3%, FPKM > 4 in neural progenitors (23)). *E*, representative ATAC-Seq and RNA-Seq tracks for the genes in P14 WT and mKO cortical cells shown in *C*, accompanied by HMGN2 ChIP-Seq (*line 3*) for neural progenitor cells, histone H3 Lys-4 methylation (*line 1*) and histone H3 Lys-27 acetylation (*line 2*) ChIP-Seq data, DNase-Seq (*line 4*) data for E14.5 whole-brain from ENCODE, and predicted binding sites for KLF7 (*blue*), RBPJ (*red*), RXR (*black*), and NFYA (*green*).

cortical cells, especially at the promoters of genes responsible for proliferation and cell polarity.

Humans and mice are conserved in genome and brain structure, which is often the basis for making mouse models to study the etiology of human diseases. For example, KO mouse models of primary microcephaly-associated genes were generated to study the cellular and molecular mechanisms underlying human microcephaly. However, the divergence between the two species results in differences in phenotypes in some of the mouse models. Consequently, investigators have often confused "microcephaly" with "significant reduction of brain size." A recent study reports that a ferret model with ASPM knockout manifested patient-like microcephaly better than mouse models, as it has normal radial expansion of the neocortex but reduced lateral cortical expansion (2). By carefully measuring the S.D. in brain size of dozens of WT mouse brains and comparing it with *Hmgn2*-KO brains according to the human definition of microcephaly (4), we showed that the *Hmgn2*-KO brain not only had a "significant reduction of size," but also exhibited "microcephaly." The microcephalic KO brain showed impaired lateral expansion and almost normal radial expansion similar to the ferret model. As ferrets are much bigger, more expensive, and have a longer lifespan, the *Hmgn2*-KO mice model offers a better option to study the etiology of microcephaly.

The investigators in the *ASPM*-KO ferret study observed the premature displacement of ventricular radial glia to the outer subventricular zone and suggest that this is the cellular mechanism that drives human primary microcephaly (2). However, it is not clear what is the cellular cause of the displacement, and it would be interesting to know how the increase of total neural progenitor cells caused microcephaly in ferrets. Here, we found a cellular phenotype of marked displacement of $PAX6^+$ $EOMES^+$ transitional cells and IPCs occurring in E18.5 mKO cortex, which is similar to that found in the ASPM-KO ferret. Importantly, we found prolonged mitosis of RGCs and decreased expression of many stem cell proliferation genes in the mKO brain, explaining how the apparent increase in the number of progenitor cells causes microcephaly. Furthermore, we found altered spindle orientation in mKO RGs, which may trigger the detachment of progenitor cells and the decreased self-renewal of RGCs. Consistently, altered spindle orientation, detached progenitor cells, and increased M-phase RGCs are also observed in many other mouse models of primary microcephaly (47–49). Thus, our *Hmgn2*-KO mouse model bridges the gap between the cellular behaviors of the human-like ferret model and the cellular mechanism of many mouse models for primary microcephaly.

Although chromatin remodelers are known to be required for the maintenance of radial glia, the notion that embryonic RG differentiation is driven by global restriction of the chromatin state is not well-established, because the tools measuring global chromatin state are quite limited (14, 15). By using ATAC-Seq for the easy capture of open chromatin regions

genome-wide in WT and mKO cells and integrating the ChIP-Seq and RNA-Seq data, we supported this idea by showing that the ablation of *Hmgn2* induced a dramatic reduction of chromatin accessibility and increased RG-to-IPC transition. Cell type–specific ATAC-Seq will be required in future studies, although fresh RG and IPCs cannot be differentiated by flow cytometry at present due to the limitation of cell surface markers.

The most-studied HMG family members, HMGAs and HMGBs, are known to control transcription and epigenetics through regulation of chromatin. HMGAs bind to AT- rich regions of the minor groove of the DNA, compete, and displace linker histone H1 from the chromatin, thus unfolding the chromatin (50). HMGBs bind to DNA without sequence specificity and remodel nucleosomes by binding and remodeling various ATP-dependent chromatin-remodeling machineries as well as histone chaperones (51). HMGNs modulate transcription in complex ways. They bind only nucleosomal DNAs mainly at open chromatins without sequence specificity, but in a tissue-specific manner (52). HMGNs regulate transcription by competing with histone H1 for its targets, by affecting histone modifications, by inhibiting ATP-dependent chromatin remodeling, or by specific interactions with certain transcription factors; all of these could result in either transcription enhancement or inhibition (52). The binding specificity of HMGN2 in embryonic neural progenitors and its roles in regulating transcription globally and locally were quite elusive before. By careful examination of the multi-omics data, we identify that in embryonic neural progenitor cells, from a global view, HMGN2 is predominantly located at promoter regions, and the binding sites are abundant in motifs of several TFs functioning during RGC development. The occupancy of HMGN2 thereby maintains global chromatin accessibility, keeping genes transcriptionally activated or repressed in a similar amount. At the level of individual genes, we pinpoint three potential direct targets of HMGN2 in RGC and propose that HMGN2 preserves transcriptional activation of these genes by keeping chromatin accessibility at their promoters to allow control of governing TFs. These in-depth analyses enrich the current understanding of transcriptional control through regulation of chromatin architecture.

Our study encountered a situation not rare but much less reported: incomplete penetrance and variable expressivity. Not all of the *Hmgn2*-deficient mice meet the criteria of microcephaly, although mouse models of other microcephaly-associated genes have similar problems (9, 10, 53). This limitation prevented us from linking the genotype of *Hmgn2* depletion to the microcephalic phenotype at earlier neurogenic stages, as the majority of KO brains were not far smaller than the mean of the WT by E18.5. This relatively mild embryonic phenotype could be explained by the tolerance and redundancy of the genome, as patients carrying the same mutations have different types and levels of brain malformation (54–56). Another explanation is functional redundancy in the HMGN family. HMGN1 and HMGN2 normally target different genes but can compensate for the binding to chromatin for each other to maintain the chromatin landscape without being up-regulated in embryonic stem cells and mouse embryonic fibroblasts (17). A further analysis of double or triple knockout of *Hmgns* would help illuminate the functional role of HMGNs in cortical neurogenesis. In conclusion, our work demonstrates that HMGN2 promotes lateral cortical expansion by maintaining global chromatin accessibility against microcephaly.

Experimental procedures

Biological samples

Human brain samples at GW14 were obtained from a tissue bank in Beijing Tian Tan Hospital of Capital Medical University, following the instructions of Tian Tan Hospital and approved by the Institutional Review Board of Tsinghua University (Project 20160013). The study abides by the Declaration of Helsinki principles.

Animals and plasmid construction

The *Hmgn2*$^{tm1a(KOMP)Wtsi}$ line was generated by the Knockout Mouse Project (KOMP) Repository of the University of California (Davis, CA) (24). All of the information of this knockout-first construct has been published online. Briefly, in the target allele, the first intron was substituted by the *FRT-En2SA (splicing acceptor)-IRES-LacZ-poly(A)-loxP-hbactP-neo-poly(A)-FRT-loxP* cassette, and a third loxP was inserted in the sixth intron, so that only the first 5 amino acids of HMGN2 could be fused with lacZ and expressed. The *Hmgn2* heterozygote strain was created on the C57BL/6N background. Sperm of heterozygotic mice was purchased from KOMP, and *in vitro* fertilization was conducted in the animal care facility at the Center of Biomedical Analysis in Tsinghua University, with C57BL/6J females as egg donors. The mutant allele was then kept in the C57BL/6J strain by subsequent mating with C57BL/6J WT mice. Only progeny from inbred heterozygotic mice were tested for genotype distribution. As mKO mice were a subpopulation of the progeny of inbred heterozygotic mice, to increase the numbers of mKO mice, KO mice were also generated from pairs of apparently normal KO parents. WT mice were generated in a similar way.

Mice were bred and kept in the animal care facility at the Center of Biomedical Analysis in Tsinghua University. All animal protocols were approved by the IACUC of Tsinghua University and conducted in accordance with guidelines of the IACUC. The laboratory animal facility of Tsinghua University has been accredited by the Association for Assessment and Accreditation of Laboratory Animal Care International. For staging embryos, the day when a vaginal plug was detected before noon was defined as E0.5. All adult mice used were between 6 and 12 weeks old, and the postnatal ages of pups are indicated throughout. PBase (to provide transposase) and PB-IRES-EGFP plasmids were constructed as described previously in the experimental procedures (57).

Immunostaining

Embryonic heads (E10.5–E18.5) were fixed at 4 °C in 4% paraformaldehyde (PFA) in 0.1 M PBS overnight. Postnatal pups and adults were perfused transcardially with PBS and then 4% PFA, followed by post-fixation of isolated brains in 4% PFA overnight at 4 °C. After fixation, the brains were equilibrated in 30% sucrose and then embedded and frozen in Tissue Tek OCT

(Sakura Finetek, Torrance, CA) for cryosectioning. Coronal cryostat sections were cut at 20 μm for embryonic tissue and at 50 μm for postnatal brain.

For staining, citrate buffer antigen retrieval was applied to the sections using the solutions (catalog no. P0088 or P0083) following the manufacturer's protocols (Beyotime). Then the cryosections were blocked in 5% BSA/PBST (1× PBS and 0.3% Triton X-100) and incubated with primary antibodies at 4 °C for 2 days. After washing with PBST, the sections were incubated with fluorescence-conjugated secondary antibodies (Alexa Fluor) overnight and then mounted with Fluoromount GTM (SouthernBiotech). The antibodies are listed in Table S1.

Image analysis and cell counting

Images were acquired using a slide scanner for fluorescence (Zeiss Axio Scan, Z1), laser-scanning confocal microscopes (Zeiss LSM710 or LSM780 or Leica TCS SP5), or the cameras on a smartphone (iPhone 7 Plus). Images were analyzed using Zeiss software ZEN2 or ImageJ. Figures were processed using Microsoft PowerPoint and assembled with Adobe Illustrator CC 2017. Total marker-positive cells were counted in 1–4 sections (two imaging fields per section) in regions that were anatomically matched between experimental groups.

Cell dissociation

Brain cortices were dissected and digested into a single-cell suspension using 10 units/ml papain (Worthington, catalog no. LS003126) for 30 min at 37 °C in Dulbecco's modified Eagle's medium as described previously (57).

Western blotting

Single cells dissociated from E14.5 cortices were washed with PBS twice and then lysed with 1% NP-40 lysis buffer (50 mM Tris-HCl (pH 7.9), 150 mM NaCl, 1% NP-40, protease inhibitor mixture (Sigma, catalog no. P8340)) on a rotator at 4 °C for 3–5 h. Protein extract was further immunoblotted against HMGN2 (rabbit monoclonal, 1:20,000, CST, catalog no. 9437S) and β-actin (mouse monoclonal, 1:5000, CWBIO, catalog no. CW0264). Goat anti-mouse IgG, HRP-conjugated (1:10,000, CWBIO, catalog no. CW0102S) and goat anti-rabbit IgG, HRP-conjugated (1:10,000, CWBIO, catalog no. CW0103S) were used as secondary antibodies.

BrdU labeling and detection

BrdU (50 mg/kg) was injected intraperitoneally into pregnant mice to label S-phase cells of E15.5 embryos. At postnatal day 14, the litters were sacrificed, perfused, and fixed. Brains were removed and cryosectioned. Frozen sections were processed for detection of BrdU (after 2 N HCl treatment) using immunofluorescence.

In utero electroporation

Timed-pregnant mice were anesthetized with isoflurane and kept warm on a heated pad. The uterine horns were exposed, and 0.5–1 μl of plasmid solution (2–3 mg/ml) was injected into the lateral ventricle of the E15.5 brain with a fine glass micropipette. Embryonic heads were then clamped between tweezer-type disc electrodes 5 mm in diameter (LF650P5; BEX). Five 36-V electrical pulses lasting 50 ms at intervals of 999 ms were delivered using an electroporator (CUY21VIVO-SQ; BEX). The uterus was then returned to the abdominal cavity to allow normal embryonic development. The phenotypes were analyzed at P14.

ATAC-Seq and RNA-Seq

WT or mKO brains at P14 were sliced on a vibratome in hibernation medium (58). Only cortices dorsal to the hippocampus between Bregma −0.22 to −2.7 were isolated. These cortices were digested into a single-cell suspension for further library preparation. The sequencing depth was 7.4–30 million reads for each replicate.

For RNA-Seq, cells were lysed with 1 ml of TRIzol reagent (Life Technologies, Inc., catalog no. 15596018) according to the manufacturer's instructions. Library construction and sequencing were conducted by ORI-GENE using the NEB Next Ultra Directional RNA Library Prep Kit for Illumina and the HiSeq X Ten System. The sequencing depth was between 46.0 and 134.9 million reads for each replicate.

For ATAC-Seq, cells were further washed twice. Five thousand cells were used for ATAC-Seq library preparation, as described previously, with minor modifications (59). In brief, samples were lysed in lysis buffer (10 mM Tris-HCl (pH 7.4), 10 mM NaCl, 3 mM $MgCl_2$, 0.1% NP-40, and protease inhibitor mixture (Sigma, P8340) for 10 min on ice to prepare nuclei. The nuclei were then spun at 700 × *g* for 3 min to remove the supernatant. They were then incubated with the Tn5 transposome solution (Vazyme Biotech) at 37 °C for 45 min. Stop buffer was added directly into the reaction to end the tagmentation. PCR was performed to amplify the library for 12 cycles according to the manufacturer's instructions. Libraries were selected with 1.2× AMPure (Beckman) beads after PCR and then sequenced on Illumina Hiseq X Ten System following the manufacturer's instructions.

Bioinformatics

FastQC and Cutadapt were used for filtering and trimming RNA-Seq reads for further analysis. Reads were aligned to the mouse genome (UCSC mm10) with hisat2 and SAMtools for RNA-Seq and with Bowtie2 for ATAC-Seq and ChIP-Seq. Stringtie and DESeq2 were used for assembling transcripts and analyzing the differential expression of genes. The differentially expressed genes (DEGs) were identified using a threshold of FDR ≤ 0.05 with $|\log_2(\text{-fold change})| > 1$.

Peak calling of ATAC-Seq and ChIP-Seq was performed using MACS. DeepTools was used to analyze and visualize ATAC-Seq signals around transcription start sites. The gene ontology (GO) enrichment analysis of DEGs was performed using DAVID (https://david.ncifcrf.gov/) (60, 61). GSEA (http://software.broadinstitute.org/gsea/index.jsp)[6] (62) was performed using all genes expressed with default parameters (permutation number = 1000, "log2_ratio_of_classes" to calculate ranking of the genes). The criteria of significant enrichment

[6] Please note that the JBC is not responsible for the long-term archiving and maintenance of this site or any other third party hosted site.

were determined as NES >1, p value < 0.05, and FDR < 0.05. To visualize the ATAC-Seq, ChIP-Seq, and RNA-Seq signals in the Integrative Genomics Viewer, we extended each read by 100 bp and calculated the coverage for each base.

De novo motif analysis was conducted using HOMER/HOMER2. The predicted binding sites for KLF7 (PB0143.1_Klf7_2/Jaspar), RBPJ (MA1116.1/Jaspar), RXR (GSE13511/Homer) and NFYA (MA0060.3/Jaspar) in mice were screened around genes of interest using HOMER. Each top ~25,000 binding sites for KLF7, RBPJ, and NFYA were accepted, whereas all were accepted for RXR. Predicted binding sequences were visualized by the Integrative Genomics Viewer.

Quantification and statistical analysis

Sequencing data were analyzed based on the negative binomial distribution, whereas data characterizing cellular phenotypes were assumed to follow normal distribution without formal tests. For Figs. 2*C* and 4*L*, the χ^2 test was used for comparisons. Other statistical analyses were performed using Prism (GraphPad Software) with unpaired Student's t test except for Fig. 2*E*, where paired Student's t test was used. Unless otherwise stated, data are presented as mean ± S.E. $p < 0.05$ was considered significant. The replicate numbers for each graph are stated in the figure legends.

Author contributions—X.-L. G., W.-J. T., and Q. S. conceptualization; X.-L. G. and W.-J. T. resources; X.-L. G., W.-J. T., B. L., and J. W. data curation; X.-L. G. and W.-J. T. formal analysis; X.-L. G., W. X., and Q. S. supervision; X.-L. G., W.-J. T., and Q. S. funding acquisition; X.-L. G. and W.-J. T. validation; X.-L. G. and W.-J. T. investigation; X.-L. G. and W.-J. T. visualization; X.-L. G. and W.-J. T. writing-original draft; X.-L. G. and Q. S. project administration; X.-L. G., W.-J. T., B. L., J. W., W. X., and Q. S. writing-review and editing; B. L., J. W., and Q. S. methodology.

Acknowledgments—We thank Dr. He Chen for helping with bioinformatics; Dr. Songhai Shi for help with laboratory facilities, reagents, and advice on project; Dr. Michael Bustin for sharing ChIP-Seq data; and Dr. Iain C. Bruce for reading the manuscript.

References

1. Götz, M., and Huttner, W. B. (2005) The cell biology of neurogenesis. *Nat. Rev. Mol. Cell Biol.* **6,** 777–788 CrossRef Medline
2. Johnson, M. B., Sun, X., Kodani, A., Borges-Monroy, R., Girskis, K. M., Ryu, S. C., Wang, P. P., Patel, K., Gonzalez, D. M., Woo, Y. M., Yan, Z., Liang, B., Smith, R. S., Chatterjee, M., Coman, D., *et al.* (2018) Aspm knockout ferret reveals an evolutionary mechanism governing cerebral cortical size. *Nature* **556,** 370–375 CrossRef Medline
3. Wang, Q., and Margolis, B. (2007) Apical junctional complexes and cell polarity. *Kidney Int.* **72,** 1448–1458 CrossRef Medline
4. Kaindl, A. M., Passemard, S., Kumar, P., Kraemer, N., Issa, L., Zwirner, A., Gerard, B., Verloes, A., Mani, S., and Gressens, P. (2010) Many roads lead to primary autosomal recessive microcephaly. *Prog. Neurobiol.* **90,** 363–383 CrossRef Medline
5. Yngvadottir, B., Xue, Y., Searle, S., Hunt, S., Delgado, M., Morrison, J., Whittaker, P., Deloukas, P., and Tyler-Smith, C. (2009) A genome-wide survey of the prevalence and evolutionary forces acting on human nonsense SNPs. *Am. J. Hum. Genet.* **84,** 224–234 CrossRef Medline
6. Xue, Y., Chen, Y., Ayub, Q., Huang, N., Ball, E. V., Mort, M., Phillips, A. D., Shaw, K., Stenson, P. D., Cooper, D. N., Tyler-Smith, C., and 1000 Genomes Project Consortium (2012) Deleterious- and disease-allele prevalence in healthy individuals: insights from current predictions, mutation databases, and population-scale resequencing. *Am. J. Hum. Genet.* **91,** 1022–1032 CrossRef Medline
7. Handsaker, R. E., Van Doren, V., Berman, J. R., Genovese, G., Kashin, S., Boettger, L. M., and McCarroll, S. A. (2015) Large multiallelic copy number variations in humans. *Nat. Genet.* **47,** 296–303 CrossRef Medline
8. Desir, J., Cassart, M., David, P., Van Bogaert, P., and Abramowicz, M. (2008) Primary microcephaly with ASPM mutation shows simplified cortical gyration with antero-posterior gradient pre- and post-natally. *Am. J. Med. Genet. A* **146A,** 1439–1443 CrossRef Medline
9. Pulvers, J. N., Bryk, J., Fish, J. L., Wilsch-Bräuninger, M., Arai, Y., Schreier, D., Naumann, R., Helppi, J., Habermann, B., Vogt, J., Nitsch, R., Tóth, A., Enard, W., Pääbo, S., and Huttner, W. B. (2010) Mutations in mouse Aspm (abnormal spindle-like microcephaly associated) cause not only microcephaly but also major defects in the germline. *Proc. Natl. Acad. Sci. U.S.A.* **107,** 16595–16600 CrossRef Medline
10. Jayaraman, D., Kodani, A., Gonzalez, D. M., Mancias, J. D., Mochida, G. H., Vagnoni, C., Johnson, J., Krogan, N., Harper, J. W., Reiter, J. F., Yu, T. W., Bae, B. I., and Walsh, C. A. (2016) Microcephaly proteins Wdr62 and Aspm define a mother centriole complex regulating centriole biogenesis, apical complex, and cell fate. *Neuron* **92,** 813–828 CrossRef Medline
11. Hirabayashi, Y., Suzki, N., Tsuboi, M., Endo, T. A., Toyoda, T., Shinga, J., Koseki, H., Vidal, M., and Gotoh, Y. (2009) Polycomb limits the neurogenic competence of neural precursor cells to promote astrogenic fate transition. *Neuron* **63,** 600–613 CrossRef Medline
12. Nishino, J., Kim, I., Chada, K., and Morrison, S. J. (2008) Hmga2 promotes neural stem cell self-renewal in young but not old mice by reducing p16Ink4a and p19Arf expression. *Cell* **135,** 227–239 CrossRef Medline
13. de la Torre-Ubieta, L., Stein, J. L., Won, H., Opland, C. K., Liang, D., Lu, D., and Geschwind, D. H. (2018) The dynamic landscape of open chromatin during human cortical neurogenesis. *Cell* **172,** 289–304.e18 CrossRef Medline
14. Kishi, Y., Fujii, Y., Hirabayashi, Y., and Gotoh, Y. (2012) HMGA regulates the global chromatin state and neurogenic potential in neocortical precursor cells. *Nat. Neurosci.* **15,** 1127–1133 CrossRef Medline
15. Zhu, J., Adli, M., Zou, J. Y., Verstappen, G., Coyne, M., Zhang, X., Durham, T., Miri, M., Deshpande, V., De Jager, P. L., Bennett, D. A., Houmard, J. A., Muoio, D. M., Onder, T. T., Camahort, R., *et al.* (2013) Genome-wide chromatin state transitions associated with developmental and environmental cues. *Cell* **152,** 642–654 CrossRef Medline
16. Deng, T., Postnikov, Y., Zhang, S., Garrett, L., Becker, L., Rácz, I., Hölter, S. M., Wurst, W., Fuchs, H., Gailus-Durner, V., de Angelis, M. H., and Bustin, M. (2017) Interplay between H1 and HMGN epigenetically regulates OLIG1&2 expression and oligodendrocyte differentiation. *Nucleic Acids Res.* **45,** 3031–3045 CrossRef Medline
17. Deng, T., Zhu, Z. I., Zhang, S., Postnikov, Y., Huang, D., Horsch, M., Furusawa, T., Beckers, J., Rozman, J., Klingenspor, M., Amarie, O., Graw, J., Rathkolb, B., Wolf, E., Adler, T., *et al.* (2015) Functional compensation among HMGN variants modulates the DNase I hypersensitive sites at enhancers. *Genome Res.* **25,** 1295–1308 CrossRef Medline
18. Huang, N., Lee, I., Marcotte, E. M., and Hurles, M. E. (2010) Characterising and predicting haploinsufficiency in the human genome. *PLoS Genet.* **6,** e1001154 CrossRef Medline
19. Lek, M., Karczewski, K. J., Minikel, E. V., Samocha, K. E., Banks, E., Fennell, T., O'Donnell-Luria, A. H., Ware, J. S., Hill, A. J., Cummings, B. B., Tukiainen, T., Birnbaum, D. P., Kosmicki, J. A., Duncan, L. E., Estrada, K., *et al.* (2016) Analysis of protein-coding genetic variation in 60,706 humans. *Nature* **536,** 285–291 CrossRef Medline
20. Firth, H. V., Richards, S. M., Bevan, A. P., Clayton, S., Corpas, M., Rajan, D., Van Vooren, S., Moreau, Y., Pettett, R. M., and Carter, N. P. (2009) DECIPHER: database of chromosomal imbalance and phenotype in humans using Ensembl resources. *Am. J. Hum. Genet.* **84,** 524–533 CrossRef Medline
21. Kugler, J. E., Deng, T., and Bustin, M. (2012) The HMGN family of chromatin-binding proteins: dynamic modulators of epigenetic processes. *Biochim. Biophys. Acta* **1819,** 652–656 CrossRef Medline
22. Dickinson, M. E., Flenniken, A. M., Ji, X., Teboul, L., Wong, M. D., White, J. K., Meehan, T. F., Weninger, W. J., Westerberg, H., Adissu, H., Baker, C. N., Bower, L., Brown, J. M., Caddle, L. B., Chiani, F., *et al.* (2016) High-

throughput discovery of novel developmental phenotypes. *Nature* **537,** 508–514 CrossRef Medline
23. Florio, M., Albert, M., Taverna, E., Namba, T., Brandl, H., Lewitus, E., Haffner, C., Sykes, A., Wong, F. K., Peters, J., Guhr, E., Klemroth, S., Prufer, K., Kelso, J., Naumann, R., *et al.* (2015) Human-specific gene ARHGAP11B promotes basal progenitor amplification and neocortex expansion. *Science* **347,** 1465–1470 CrossRef Medline
24. Austin, C. P., Battey, J. F., Bradley, A., Bucan, M., Capecchi, M., Collins, F. S., Dove, W. F., Duyk, G., Dymecki, S., Eppig, J. T., Grieder, F. B., Heintz, N., Hicks, G., Insel, T. R., Joyner, A., *et al.* (2004) The knockout mouse project. *Nat. Genet.* **36,** 921–924 CrossRef Medline
25. Brown, S. D. M., Holmes, C. C., Mallon, A. M., Meehan, T. F., Smedley, D., and Wells, S. (2018) High-throughput mouse phenomics for characterizing mammalian gene function. *Nat. Rev. Genet.* **19,** 357–370 CrossRef Medline
26. Griffiths, A. J. F. (2000) *An Introduction to Genetic Analysis*, 7th Ed., W.H. Freeman, New York
27. Chen, F., and LoTurco, J. (2012) A method for stable transgenesis of radial glia lineage in rat neocortex by piggyBac mediated transposition. *J. Neurosci. Methods* **207,** 172–180 CrossRef Medline
28. Kriegstein, A., and Alvarez-Buylla, A. (2009) The glial nature of embryonic and adult neural stem cells. *Annu. Rev. Neurosci.* **32,** 149–184 CrossRef Medline
29. Semple, B. D., Blomgren, K., Gimlin, K., Ferriero, D. M., and Noble-Haeusslein, L. J. (2013) Brain development in rodents and humans: Identifying benchmarks of maturation and vulnerability to injury across species. *Prog. Neurobiol.* **106,** 1–16 CrossRef Medline
30. Siller, K. H., and Doe, C. Q. (2009) Spindle orientation during asymmetric cell division. *Nat. Cell Biol.* **11,** 365–374 CrossRef Medline
31. Buenrostro, J. D., Giresi, P. G., Zaba, L. C., Chang, H. Y., and Greenleaf, W. J. (2013) Transposition of native chromatin for fast and sensitive epigenomic profiling of open chromatin, DNA-binding proteins and nucleosome position. *Nat. Methods* **10,** 1213–1218 CrossRef Medline
32. Singh, S., and Solecki, D. J. (2015) Polarity transitions during neurogenesis and germinal zone exit in the developing central nervous system. *Front. Cell Neurosci.* **9,** 62 CrossRef Medline
33. Moon, B. S., Bai, J., Cai, M., Liu, C., Shi, J., and Lu, W. (2018) Kruppel-like factor 4-dependent Staufen1-mediated mRNA decay regulates cortical neurogenesis. *Nat. Commun.* **9,** 401 CrossRef Medline
34. Ramasamy, S. K., and Lenka, N. (2010) Notch exhibits ligand bias and maneuvers stage-specific steering of neural differentiation in embryonic stem cells. *Mol. Cell. Biol.* **30,** 1946–1957 CrossRef Medline
35. Liu, Y., Gupta, G. D., Barnabas, D. D., Agircan, F. G., Mehmood, S., Wu, D., Coyaud, E., Johnson, C. M., McLaughlin, S. H., Andreeva, A., Freund, S. M. V., Robinson, C. V., Cheung, S. W. T., Raught, B., Pelletier, L., and van Breugel, M. (2018) Direct binding of CEP85 to STIL ensures robust PLK4 activation and efficient centriole assembly. *Nat. Commun.* **9,** 1731 CrossRef Medline
36. Lee, J. E., Hollenberg, S. M., Snider, L., Turner, D. L., Lipnick, N., and Weintraub, H. (1995) Conversion of *Xenopus* ectoderm into neurons by Neurod, a basic helix-loop-helix protein. *Science* **268,** 836–844 CrossRef Medline
37. Olson, J. M., Asakura, A., Snider, L., Hawkes, R., Strand, A., Stoeck, J., Hallahan, A., Pritchard, J., and Tapscott, S. J. (2001) NeuroD2 is necessary for development and survival of central nervous system neurons. *Dev. Biol.* **234,** 174–187 CrossRef Medline
38. Ochocinska, M. J., and Hitchcock, P. F. (2009) NeuroD regulates proliferation of photoreceptor progenitors in the retina of the zebrafish. *Mech. Dev.* **126,** 128–141 CrossRef Medline
39. Laub, F., Lei, L., Sumiyoshi, H., Kajimura, D., Dragomir, C., Smaldone, S., Puche, A. C., Petros, T. J., Mason, C., Parada, L. F., and Ramirez, F. (2005) Transcription factor KLF7 is important for neuronal morphogenesis in selected regions of the nervous system. *Mol. Cell. Biol.* **25,** 5699–5711 CrossRef Medline
40. Kajimura, D., Dragomir, C., Ramirez, F., and Laub, F. (2007) Identification of genes regulated by transcription factor KLF7 in differentiating olfactory sensory neurons. *Gene* **388,** 34–42 CrossRef Medline
41. Hitoshi, S., Alexson, T., Tropepe, V., Donoviel, D., Elia, A. J., Nye, J. S., Conlon, R. A., Mak, T. W., Bernstein, A., and van der Kooy, D. (2002) Notch pathway molecules are essential for the maintenance, but not the generation, of mammalian neural stem cells. *Genes Dev.* **16,** 846–858 CrossRef Medline
42. Mounier, A., Georgiev, D., Nam, K. N., Fitz, N. F., Castranio, E. L., Wolfe, C. M., Cronican, A. A., Schug, J., Lefterov, I., and Koldamova, R. (2015) Bexarotene-activated retinoid X receptors regulate neuronal differentiation and dendritic complexity. *J. Neurosci.* **35,** 11862–11876 CrossRef Medline
43. Siegenthaler, J. A., Ashique, A. M., Zarbalis, K., Patterson, K. P., Hecht, J. H., Kane, M. A., Folias, A. E., Choe, Y., May, S. R., Kume, T., Napoli, J. L., Peterson, A. S., and Pleasure, S. J. (2009) Retinoic acid from the meninges regulates cortical neuron generation. *Cell* **139,** 597–609 CrossRef Medline
44. Yamanaka, T., Tosaki, A., Kurosawa, M., Matsumoto, G., Koike, M., Uchiyama, Y., Maity, S. N., Shimogori, T., Hattori, N., and Nukina, N. (2014) NF-Y inactivation causes atypical neurodegeneration characterized by ubiquitin and p62 accumulation and endoplasmic reticulum disorganization. *Nat. Commun.* **5,** 3354 CrossRef Medline
45. Oldfield, A. J., Yang, P., Conway, A. E., Cinghu, S., Freudenberg, J. M., Yellaboina, S., and Jothi, R. (2014) Histone-fold domain protein NF-Y promotes chromatin accessibility for cell type-specific master transcription factors. *Mol. Cell* **55,** 708–722 CrossRef Medline
46. Bhattacharya, A., Deng, J. M., Zhang, Z., Behringer, R., de Crombrugghe, B., and Maity, S. N. (2003) The B subunit of the CCAAT box binding transcription factor complex (CBF/NF-Y) is essential for early mouse development and cell proliferation. *Cancer Res.* **63,** 8167–8172 Medline
47. Chen, J.-F., Zhang, Y., Wilde, J., Hansen, K. C., Lai, F., and Niswander, L. (2014) Microcephaly disease gene Wdr62 regulates mitotic progression of embryonic neural stem cells and brain size. *Nat. Commun.* **5,** 3885 CrossRef Medline
48. Gruber, R., Zhou, Z., Sukchev, M., Joerss, T., Frappart, P. O., and Wang, Z. Q. (2011) MCPH1 regulates the neuroprogenitor division mode by coupling the centrosomal cycle with mitotic entry through the Chk1-Cdc25 pathway. *Nat. Cell Biol.* **13,** 1325–1334 CrossRef Medline
49. Insolera, R., Bazzi, H., Shao, W., Anderson, K. V., and Shi, S. H. (2014) Cortical neurogenesis in the absence of centrioles. *Nat. Neurosci.* **17,** 1528–1535 CrossRef Medline
50. Ozturk, N., Singh, I., Mehta, A., Braun, T., and Barreto, G. (2014) HMGA proteins as modulators of chromatin structure during transcriptional activation. *Front. Cell Dev. Biol.* **2,** 5 CrossRef Medline
51. Malarkey, C. S., and Churchill, M. E. (2012) The high mobility group box: the ultimate utility player of a cell. *Trends Biochem. Sci.* **37,** 553–562 CrossRef Medline
52. Zhu, N., and Hansen, U. (2010) Transcriptional regulation by HMGN proteins. *Biochim. Biophys. Acta* **1799,** 74–79 CrossRef Medline
53. Dupuis, N., Fafouri, A., Bayot, A., Kumar, M., Lecharpentier, T., Ball, G., Edwards, D., Bernard, V., Dournaud, P., Drunat, S., Vermelle-Andrzejewski, M., Vilain, C., Abramowicz, M., Désir, J., Bonaventure, J., *et al.* (2015) Dymeclin deficiency causes postnatal microcephaly, hypomyelination and reticulum-to-Golgi trafficking defects in mice and humans. *Hum. Mol. Genet.* **24,** 2771–2783 CrossRef Medline
54. Manzini, M. C., and Walsh, C. A. (2011) What disorders of cortical development tell us about the cortex: one plus one does not always make two. *Curr. Opin. Genet. Dev.* **21,** 333–339 CrossRef Medline
55. Seltzer, L. E., and Paciorkowski, A. R. (2014) Genetic disorders associated with postnatal microcephaly. *Am. J. Med. Genet. C Semin. Med. Genet.* **166C,** 140–155 CrossRef Medline
56. Thornton, G. K., and Woods, C. G. (2009) Primary microcephaly: do all roads lead to Rome? *Trends Genet.* **25,** 501–510 CrossRef Medline
57. Hu, X. L., Chen, G., Zhang, S., Zheng, J., Wu, J., Bai, Q. R., Wang, Y., Li, J., Wang, H., Feng, H., Li, J., Sun, X., Xia, Q., Yang, F., Hang, J., *et al.* (2017) Persistent Expression of VCAM1 in radial glial cells is required for the embryonic origin of postnatal neural stem cells. *Neuron* **95,** 309–325.e6 CrossRef Medline
58. New, J. S., Jass, P. A., and Barrett, K. A. (1986) Preparation of Reissert compounds derived from the thieno[3,2-C]pyridine, thieno[2,3-D]pyridazine and the thieno[2,3-D]pyrimidine ring-systems. *J. Heterocycl. Chem.* **23,** 545–548 CrossRef
59. Wu, J., Huang, B., Chen, H., Yin, Q., Liu, Y., Xiang, Y., Zhang, B., Liu, B., Wang, Q., Xia, W., Li, W., Li, Y., Ma, J., Peng, X., Zheng, H., *et al.* (2016) The landscape of accessible chromatin in mammalian preimplantation embryos. *Nature* **534,** 652–657 CrossRef Medline

60. Huang, D. W, Sherman, B. T., and Lempicki, R. A. (2009) Systematic and integrative analysis of large gene lists using DAVID bioinformatics resources. *Nat. Protoc.* **4,** 44–57 CrossRef Medline
61. Huang, D. W., Sherman, B. T., and Lempicki, R. A. (2009) Bioinformatics enrichment tools: Paths toward the comprehensive functional analysis of large gene lists. *Nucleic Acids Res.* **37,** 1–13 CrossRef Medline
62. Subramanian, A., Tamayo, P., Mootha, V. K., Mukherjee, S., Ebert, B. L., Gillette, M. A., Paulovich, A., Pomeroy, S. L., Golub, T. R., Lander, E. S., and Mesirov, J. P. (2005) Gene set enrichment analysis: a knowledge-based approach for interpreting genome-wide expression profiles. *Proc. Natl. Acad. Sci. U.S.A.* **102,** 15545–15550 CrossRef Medline